

Manuscript version: Author's Accepted Manuscript

The version presented in WRAP is the author's accepted manuscript and may differ from the published version or Version of Record.

Persistent WRAP URL:

<http://wrap.warwick.ac.uk/159056>

How to cite:

Please refer to published version for the most recent bibliographic citation information.

Copyright and reuse:

The Warwick Research Archive Portal (WRAP) makes this work by researchers of the University of Warwick available open access under the following conditions.

Copyright © and all moral rights to the version of the paper presented here belong to the individual author(s) and/or other copyright owners. To the extent reasonable and practicable the material made available in WRAP has been checked for eligibility before being made available.

Copies of full items can be used for personal research or study, educational, or not-for-profit purposes without prior permission or charge. Provided that the authors, title and full bibliographic details are credited, a hyperlink and/or URL is given for the original metadata page and the content is not changed in any way.

Publisher's statement:

Please refer to the repository item page, publisher's statement section, for further information.

For more information, please contact the WRAP Team at: wrap@warwick.ac.uk.

Scanning electrochemical cell microscopy (SECCM) in a glovebox: Structure-activity correlations in the early stages of solid-electrolyte interphase (SEI) formation on graphite

Dr. Daniel Martín-Yerga^{1,3*}, Dr. Minkyung Kang^{1,2}, Prof. Patrick R. Unwin^{1,3*}

¹*Department of Chemistry, University of Warwick, Coventry CV47AL, United Kingdom*

²*Institute for Frontier Materials, Deakin University, Burwood VIC 3125, Australia*

³*The Faraday Institution, Quad One, Harwell Campus, Didcot OX11 0RA, United Kingdom*

*Corresponding authors: daniel.martin-yerga@warwick.ac.uk (D.M-Y); p.r.unwin@warwick.ac.uk (P.R.U.)

ABSTRACT

Understanding the formation and properties of the solid-electrolyte interphase (SEI) will enable the development of enhanced Li-ion batteries (LiBs) and other battery types. Herein, we report scanning electrochemical cell microscopy (SECCM) in a glovebox to characterize the SEI formation on the basal surface of highly oriented pyrolytic graphite (HOPG) as a model system of negative LiB electrodes with nonaqueous electrolytes. Different grades of HOPG have been studied, which provide a range of step edge densities on the basal surface. The high-throughput and spatially-resolved character of SECCM allows thousands of measurements across a surface, revealing how surface heterogeneity in graphite affects the early stages of the SEI formation and its properties. Step edges promote electrolyte reduction resulting in a more passivating SEI than that formed on smoother surfaces. A strongly insulating but relatively unstable SEI is detected under fast formation conditions, while slow formation rates induce the steady growth of an increasingly passivating SEI. This work provides new insights on the SEI dynamic formation and demonstrates SECCM as a powerful technique to probe the effect of local structure in heterogeneous battery materials under inert atmosphere. The demonstration that SECCM can readily be deployed in a glovebox serves as a foundation for future experiments that will explore high resolution electrochemical imaging of battery electrode materials.

KEYWORDS: Solid electrolyte interphase, Graphite, Li-ion battery, Electrochemistry, Scanning probe microscopy

INTRODUCTION

The solid electrolyte interphase (SEI) formed at the surface of negative electrodes in nonaqueous lithium-ion batteries (LiBs) is a complex layer composed by organic and inorganic Li-based species.^[1–3] Electrochemical reduction and decomposition of the electrolyte, which occurs at potentials more positive than Li^+ intercalation, is the first step of the SEI formation on graphite,^[4,5] the most common material for the negative electrode in LiBs. The physical and chemical properties of the SEI play an essential role in battery performance; ideally the SEI should provide fast Li^+ conduction, good mechanical strength and adherence and good electronic insulation (passivation) to prevent subsequent electrolyte reduction upon cycling. SEI formation is an expensive and time-consuming step in battery manufacture, as slow conditions are used to generate a dense SEI with optimal properties.^[3,6] However, the SEI in real devices is far from ideal, undergoing continuous growth upon cycling, consuming further Li^+ ions and increasing the cell impedance,^[7] all of which lead to significant performance losses in batteries.

SEI formation on graphite electrodes with nonaqueous electrolytes has been widely studied^[3,4,8,9] but many mechanistic aspects remain to be addressed. The use of new characterization techniques^[10] is revealing the strong dependence of the SEI formation and properties on factors such as electrolyte nature and concentration, presence of additives, and electrode materials and conditions.^[3,11,12] The graphite surface also plays an important role in both the Li^+ intercalation^[13,14] and the SEI formation and properties.^[15,16] It is well accepted that Li^+ intercalation in graphite takes place at step edges,^[4,17] leading to a higher (de)lithiation activity at the edge plane than at the basal plane, but studies aimed at unambiguously determining the role of step edges and terraces on the formation and properties of the SEI are ongoing.^[12,18,19]

The use of highly oriented pyrolytic graphite (HOPG) electrodes with a well-defined surface structure is a standard approach to investigate structural effects on electrochemistry at graphite.^[19–23] In many of these studies, the HOPG electrodes are configured with either basal or edge plane orientation in order to infer the gross electrochemical behaviour of step edges or terraces at the macroscale. However, most studies where HOPG electrodes were basal-plane oriented have shown significant (de)lithiation currents,^[19,20,24–26] highlighting the role of step edges on the basal surface and making it difficult to elucidate the effect of step edge coverage. Herein, we study a set of HOPG basal plane samples that provide a range of step density and use of localized techniques to provide large datasets and enable understanding of the effect of surface heterogeneity on SEI formation.

Scanning probe microscopies (SPMs) such as electrochemical scanning tunnelling microscopy (EC-STM) and atomic force microscopy (EC-AFM) have provided information about changes in the local surface of graphite electrodes under lithiation and SEI formation conditions.^[19,25–28] For example, exfoliation promoted by initial solvent co-intercalation into step edges^[27] or pit

corrosion in LiPF_6 electrolytes at long timescales^[25] have been observed. The formation of SEI insoluble components has been detected at potentials as high as +1.7 V (vs Li/Li^+),^[29] with layers reaching thicknesses of tens of nm even on the first charge/discharge cycle.^[18,26] These insoluble species appear to be deposited on step edges at more positive potentials compared to the basal surface,^[18] and a thicker^[12,19] and more adhesive^[19] SEI is also found on the step edges. Yet, despite the valuable morphological information on the SEI formation provided by these techniques, the underlying local electrochemistry (spatially-resolved current-voltage relationship) is not revealed directly.

Attempts to uncover local electrochemistry have hitherto involved the use of scanning electrochemical microscopy (SECM) to study SEI formation and evolution at a variety of carbon-based electrodes, including HOPG,^[30] glassy carbon,^[31,32] graphene^[33] and graphite composites.^[34,35] SECM has visualized spatiotemporal changes of the passivating properties of the SEI,^[35–37] formation of gas bubbles during electrolyte reduction,^[36] and some inhomogeneities in surface electroactivity along the electrode surface.^[34] However, it is important to point out that surface reactivity was measured by an additional redox mediator in solution, which essentially detects contrast between active and passive regions of the surface. Moreover, hitherto, SECM measurements of this type were recorded with relatively low spatial resolution using large microelectrode probes (diameters: 10–25 μm). A common factor of all the SPMs mentioned (EC-STM, EC-AFM, SECM) is that the electrode investigated (and the tip electrode in the case of SECM) is immersed in the electrolyte solution for long periods throughout the experiment. This is a significant consideration because graphite used as battery electrode can undergo spontaneous surface changes, even at open circuit potential,^[34] and graphite corrosion has been observed in typical LiPF_6 electrolytes by the effect of HF.^[25]

Scanning electrochemical cell microscopy (SECCM)^[38,39] has considerable potential to measure directly and locally electrochemical reactions of interest.^[40,41] SECCM uses a nanoscale probe with a confined electrolyte droplet that is placed in meniscus contact at a series of locations on a surface to carry out fast, high-throughput electrochemical measurements. SECCM has proven powerful in studying structurally heterogeneous materials with practical relevance in many fields, including electrocatalysis,^[42,43] corrosion^[44] and sensing,^[45] and its inherent features make it promising for battery electrode research. It has previously been employed to study the spatially-resolved activity and (de)lithiation of active materials used in positive battery electrodes such as LiFePO_4 composite electrodes,^[46,47] isolated LiFePO_4 microparticles^[47] and isolated LiMn_2O_4 nanoparticles, where SECCM measurements were combined with identical location electron microscopy.^[48]

The above SECCM studies all made use of aqueous electrolytes; the use of nonaqueous solvents with low viscosity, as used in batteries, has been reported as challenging to implement with

meniscus-based techniques; large droplet spread (surface wetting) has been observed.^[49,50] To address this issue the use of a gel polymer electrolyte with DMSO within the SECCM nanopipette has been reported,^[51] but a recent technical breakthrough has seen the successful employment of nonaqueous (single or mixed) solvents, where at least one of the components has a high boiling point (such as ethylene carbonate or propylene carbonate), producing a very stable meniscus contact in SECCM and highly-reproducible measurements.^[52] These developments have opened the door to apply SECCM for studies of LiBs in nonaqueous electrolytes, and recently, the (de)lithiation of positive LiCoO₂ particles and Li₄Ti₅O₁₂ thin film electrodes with organic carbonate electrolytes in a glovebox under inert atmosphere has been reported.^[53]

Herein, SECCM is employed to investigate the early stages of SEI formation on graphite negative electrodes in a typical Li-ion battery electrolyte under inert atmosphere (glovebox). Using HOPG electrodes of different quality, we show how step edge density affects the electrochemical processes that lead to SEI formation and the resulting properties of the SEI. SECCM is demonstrated to be a promising technique for providing microscopic understanding of structure-activity-property relationships in heterogeneous materials used as a model for non-aqueous batteries.

RESULTS AND DISCUSSION

Voltammetric SECCM in a glovebox

Figure 1 illustrates the SECCM setup deployed in an Ar-filled glovebox used in this work. Briefly, a single-barrel pipette (tip diameter of ~500 nm, Figure S1a) filled with 1 M LiPF₆ in ethylene carbonate (EC) – ethyl methyl carbonate (EMC), and also containing a Ag quasi-reference counter electrode (QRCE), was used as a mobile localised electrochemical probe in a hopping-mode protocol (Figure 1a). The pipette was approached towards the HOPG surface until a liquid meniscus contact was formed, whereupon a cyclic voltammogram (CV) was recorded (Figure 1b). 3D-printed pipette holders (Figure 1c) were designed to facilitate the handling, filling and mounting of the pipettes inside the glovebox. Experiments were carried out in visually smooth HOPG areas, avoiding very large steps and defects (Figure 1d). This protocol resulted in well-defined and consistent electrolyte footprints (Figure 1e), which proves that the meniscus contact from the SECCM probe with the HOPG surface was very stable under the working conditions in the glovebox. Ag QRCE potentials were converted to the Li/Li⁺ scale using the reversible one-electron oxidation of ferrocene (Fc) as a reference (Figure S2). Further experimental details are described in the experimental section.

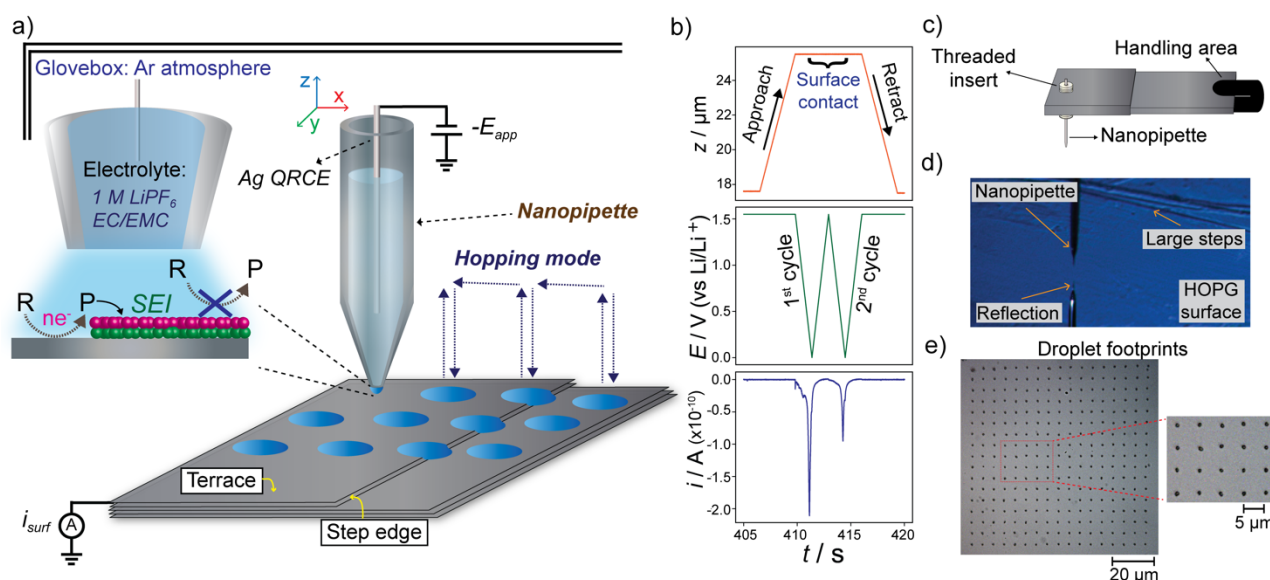


Figure 1. (a) Schematic of SECCM operated in a hopping mode to study the formation of the solid-electrolyte interphase (SEI) at HOPG electrodes. A single-channel pipette filled with 1 M LiPF₆ in EC/EMC was translated at a series of predefined positions to record spatially-resolved electrochemical measurements. Voltammetric measurements were recorded by applying a potential ($-E_{app}$) to the Ag QRCE in the tip, with respect to the HOPG working electrode, where the resulting current (i_{surf}) was measured. Ag QRCE potentials were converted to the Li/Li⁺ scale using ferrocene oxidation as a reference (Figure S2). (b) Plots representing the variation of the z-position of the pipette, the applied potential and the measured current as a function of time during a typical SECCM experiment consisting of two voltammetric cycles at a pixel (spot on the surface). (c) Schematic of a 3D-printed pipette holder used to facilitate handling of the pipette inside the glovebox. The holders have a threaded insert, which was removable to adapt the holder for pipettes with different outer diameter. (d) Optical image of a pipette probe near a ZYB HOPG surface in a basal plane orientation. Experiments were carried out in visually smooth areas avoiding any very large steps and defects. (e) Optical image of a droplet footprint left by an SECCM experiment in 1 M LiPF₆ in EC/EMC. Scan size was 80x80 μ m with 5 μ m hopping distance. A pipette probe with ca. 500 nm diameter was employed (Figure S1a).

Characterisation of HOPG electrodes

HOPG electrodes of different grade with a range of step edge densities were studied. Atomic force microscopy (AFM) images of these HOPG electrodes are shown in Figure 2. ZYA HOPG provided a basal plane with a relatively low step density and large areas comprising smooth terraces as shown in Figure 2a. There were some areas where a larger step coverage was observed (SI, Figure S3a), but the step heights were generally small, consisting mainly of 1-3 graphite layers (given a layer separation in graphite^[54] of ~ 0.335 nm). In contrast, the basal plane of ZYB HOPG had a significantly larger coverage of steps with heights ranging from 1-6 graphite layers (Figures 2b and S3b). ZYH HOPG (Figure 2c) was more heterogeneous, with a generally lower step density than ZYB HOPG, but with most of the steps formed by a higher number of graphite layers. For instance, SI, Figure S3c shows an area of ZYH HOPG where steps are formed by 13-17 graphite layers.

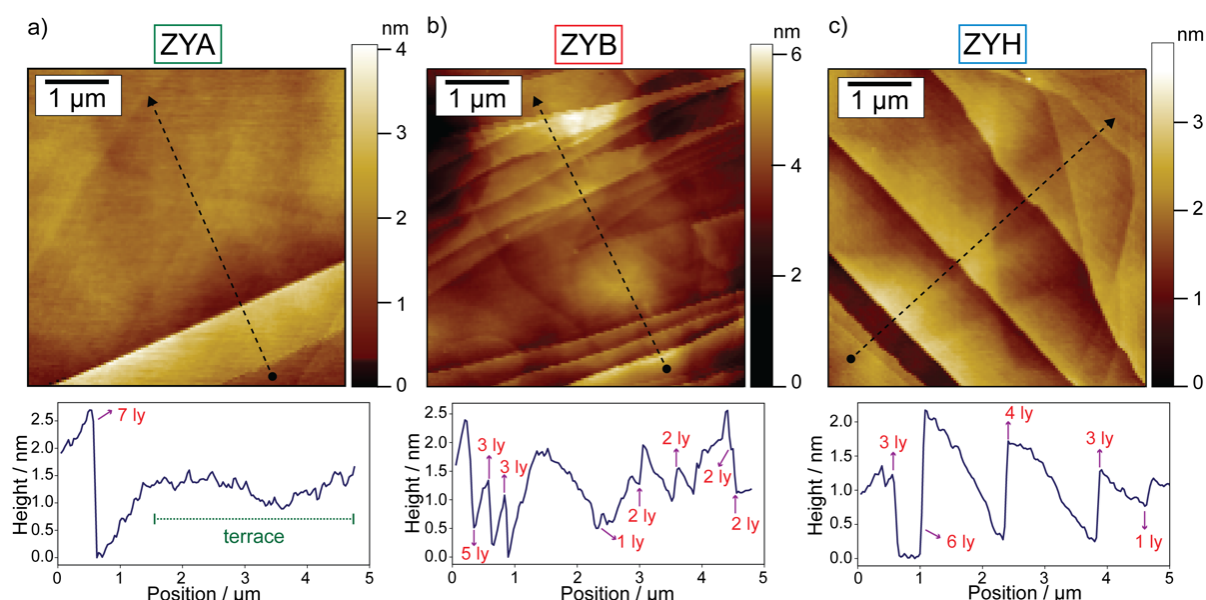


Figure 2. AFM topography images of freshly cleaved HOPG with corresponding height profiles for (a) ZYA, (b) ZYB, and (c) ZYH grades. Arrows indicate the location and direction where the height profiles were extracted. "ly" is graphite layer.

Electrolyte reactivity: the first step in solid-electrolyte interphase formation

The electrochemical behaviour of freshly-cleaved HOPG electrodes in 1 M LiPF₆ in EC/EMC was studied by spatially-resolved SECCM CV measurements. Figure 3a shows representative voltammograms recorded at a scan rate of 1 V s⁻¹. The resulting timescale is short compared to that used for SEI formation in battery manufacture, but ensures that many measurements can be made at different locations on a sample and is also interesting as it reveals SEI formation at the earliest stage.

All the HOPG electrodes (ZYA, ZYB, ZYH) showed qualitatively comparable voltammetric profiles. Two distinct regions can be discerned in the cathodic sweep: a) a low-intensity broad process (C_I) with onset and peak potentials approximately at +1.2 V and +0.7 V (vs Li/Li⁺), respectively, and b) a high-intensity, sharp and quasi-symmetric process (C_{II}) having onset and peak potentials at about +0.5 V and +0.2 V (vs Li/Li⁺), respectively. These electron-transfer processes are attributed to the electrolyte salt (LiPF₆) and solvent (EC and EMC) reduction reactions, which are the initial steps of the SEI formation. The full reaction pathway and precise composition of the SEI still remain under debate^[8,55] but there is a fair consensus regarding the initial reactions,^[5,8,56–58] including the formation of: a) LiF by decomposition and reduction of LiPF₆ related compounds (Figure S4a),^[25,59,60] b) lithium ethylene dicarbonate (LEDC) via reduction of EC (Figure S4b), although it has been proposed recently that the actual species is lithium ethylene monocarbonate (LEMC),^[55] and c) lithium methyl or ethyl carbonates (LMC, LEC) by reduction of EMC (Figure S4c), but reduction of EC seems to take place preferentially in binary EC/EMC solvents.^[61] While trying to assign the voltammetric

profile to specific electrochemical reactions might be tempting, this is challenging and contradictory results have been reported. For instance, the SEI generated at the most positive potentials was reported to be essentially comprised of organic species,^[62] inferring that solvent reduction takes place at lower overpotentials than electrolyte salt reduction, while the formation of LiF has been observed at more negative potentials,^[60] near to the C_{II} peak in Figure 3a. In contrast, an SEI with a considerable amount of inorganic species such as LiF has also been observed at potentials even more positive than +1.0 V (vs Li/Li⁺).^[63] The fact that insoluble inorganic species are preferentially found in the SEI near the electrode surface^[12,18] can also mislead as to which component is reduced first, as some of the initially formed organic species may be partially soluble,^[8,64] so they are preferentially present in the upper layer of the SEI.^[8,65] Favoured salt reduction on step edges has also been reported, as an SEI richer in inorganic species on the edge plane has been found.^[16,19,63,66] While the SECCM voltammetric profiles for the different HOPG grades were qualitatively similar, the peak magnitude of the C_{II} reduction process was strongly dependent on the HOPG grade as discussed below.

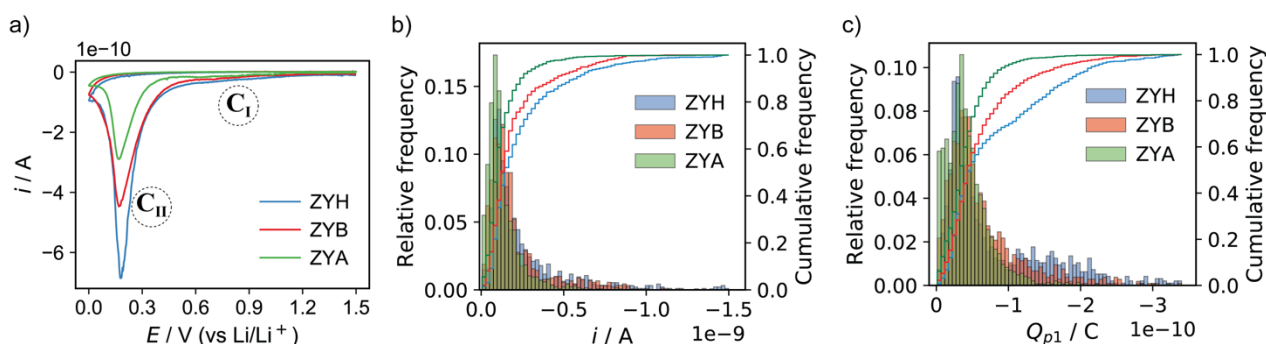


Figure 3. (a) SECCM CVs obtained for HOPG electrodes of different grades: ZYA (green line), ZYB (red line) and ZYH (blue line) in 1 M LiPF₆ in EC/EMC. C_I and C_{II} represent the two main reduction processes detected in the voltammetric profile. Scan rate was 1 V s⁻¹. (b) Population analysis illustrating the relative (histogram, left axis) and cumulative (lines, right axis) frequency of SECCM measurements as a function of the current at a potential of +0.30 V (vs Li/Li⁺) for HOPG electrodes. The width of the histogram bars is ca. 23 pA. (c) Population analysis illustrating the relative (histogram, left axis) and cumulative (lines, right axis) frequency of SECCM measurements as a function of the peak charge of the C_{II} voltammetric process for pristine HOPG electrodes. The width of the histogram bars is ca. 7 pC. Population analysis obtained from 1446, 1061 and 963 independent measurements at ZYA, ZYB and ZYH HOPG, respectively

To reveal the effect of step edge coverage on the electrolyte reduction, a population analysis of the SECCM experiments on HOPG electrodes of different quality (ZYA, ZYB, ZYH) was carried out using the C_{II} reduction process. This statistical analysis provides rich datasets based on the large number of measurements made. It is worth noting that electrolyte reduction leads to SEI formation, which subsequently inhibits that same reaction, resulting in the peak profiles seen in Figure 3a. Thus, to analyse the electrolyte reduction activity under minimal effect of the SEI passivation, the current at a potential well below the peak potential needs to be considered. In contrast, analysing the full peak

might provide some information about both related phenomena: electrolyte reduction activity and initial SEI passivation. Figure 3b shows the population analysis of SECCM measurements as a function of electrolyte reduction activity (current at +0.30 V vs Li/Li⁺, named i_1 hereafter). The electrolyte reduction activity was heterogeneous with i_1 values ranging from a few tens of pA to ca. 1.5 nA as represented in Figure 3b, which demonstrates the surface heterogeneity in HOPG (both within the surface of a particular grade, and across the grades), as also revealed by the AFM images (Figures 2 and S3). Examining differences between HOPG grades, i_1 was similar on many locations (with >50% of the measurements between 75-200 pA), but important variations can be found at limiting cases of activity. For instance, i_1 was higher (in absolute value) than 250 pA in 11% of the locations in ZYA compared to 24% in ZYB and 32% in ZYH. This fact reveals that step edges promote the electrolyte reduction, and both coverage and size of step edges, which are different in each HOPG sample, can affect these reactions. In terms of low activity, i_1 was lower than 50 pA in 15% of the locations in ZYA compared to 8% in ZYB and 3% in ZYH.

To analyse the full peak, the charge of the C_{II} reduction peak was integrated (see Figure S5), named hereafter Q_{p1} for the first voltammetric cycle. The magnitude of Q_{p1} depends on the relative rates of electrolyte reduction and SEI passivation. Figure 3c shows that the Q_{p1} population analysis on the different HOPG electrodes has a similar trend as for the electrolyte reduction activity, although the relative differences between HOPG grades are noticeably larger. For instance, Q_{p1} was higher (in absolute value) than 100 pC in 5% of the locations in ZYA, compared to 18% in ZYB and 31% in ZYH. Thus, Q_{p1} appears to be determined by electrolyte reduction before SEI passivation sets in.

It is worth noting that Li⁺ intercalation and deintercalation processes were not detected in the SECCM measurements in Figure 3a, even though there are step edges on the basal surface, which can be attributed to the relatively low abundance of step edges on the samples and the fast timescale of the measurements. These data are also consistent with the observation that Li⁺ intercalation in graphite flakes containing a small number of low-height step edges causes a high strain within the structure,^[67] which makes further Li⁺ intercalation difficult. We could only measure delithiation currents when SECCM experiments were carried out with larger micropipettes (~30 μm diameter) and covering rather large defects on the graphite basal plane (Figure S6).

Effect of graphite structure on the solid-electrolyte interphase formation

An ideal SEI layer should be strongly passivating, to prevent further electrolyte reduction after its formation. To assess the passivating properties of the initial SEI on the different HOPG materials, a study was performed comparing the first and second charge/discharge cycles, whereby the Q_p ratio between the second and first cycles (Q_{p2}/Q_{p1}) was used as a parameter to determine the passivation efficiency of the SEI layer formed during the first cycle. Figures 4a-c show representative

SECCM voltammetric responses in 3 different locations of a ZYB HOPG electrode where the passivation efficiency of the SEI was significantly different. The first case shows an electrode location where the formed SEI only blocked the electrolyte reduction slightly, with a Q_{p2}/Q_{p1} ratio of 0.66. An SEI with better passivation properties was formed in the other two locations with Q_{p2}/Q_{p1} ratios of 0.21 and 0.009, respectively. A strong relationship between the Q_{p1} absolute values and Q_{p2}/Q_{p1} or Q_{p2} is evident in these cases and will be discussed further below.

A complete population analysis of the Q_{p2}/Q_{p1} ratio from the SECCM measurements on different HOPG electrodes is shown in Figure 4d. Electrochemically heterogeneous SEI layers were detected at different locations of the HOPG surfaces, with Q_{p2}/Q_{p1} values from 0.002 (an SEI almost fully passivating) to near 1 (similar to pristine surfaces). There is an evident trend between the HOPG grade and the passivation efficiency of the SEI layer, with a higher frequency of SECCM measurements tending towards lower Q_{p2}/Q_{p1} values from ZYA to ZYH HOPG electrodes. For instance, 66%, 33% and 17% of the total measurements had a Q_{p2}/Q_{p1} above 0.2 for ZYA, ZYB and ZYH HOPG, respectively. Similarly, the measurements where the Q_{p2}/Q_{p1} values were close to zero ($Q_{p2}/Q_{p1} < 0.02$) corresponded to 2%, 7% and 13% of the total for ZYA, ZYB, and ZYH HOPG, respectively, as summarized in Figure 4e. These observations reveal that the SEI formed on HOPG with a higher coverage of step edges prevents further electrolyte reduction more effectively. In addition, the larger step edges found on ZYH HOPG also seem to promote a more protecting SEI when compared to the ZYB HOPG, so not only is the coverage of step edges important, but also their properties (such as height or number of graphite layers).

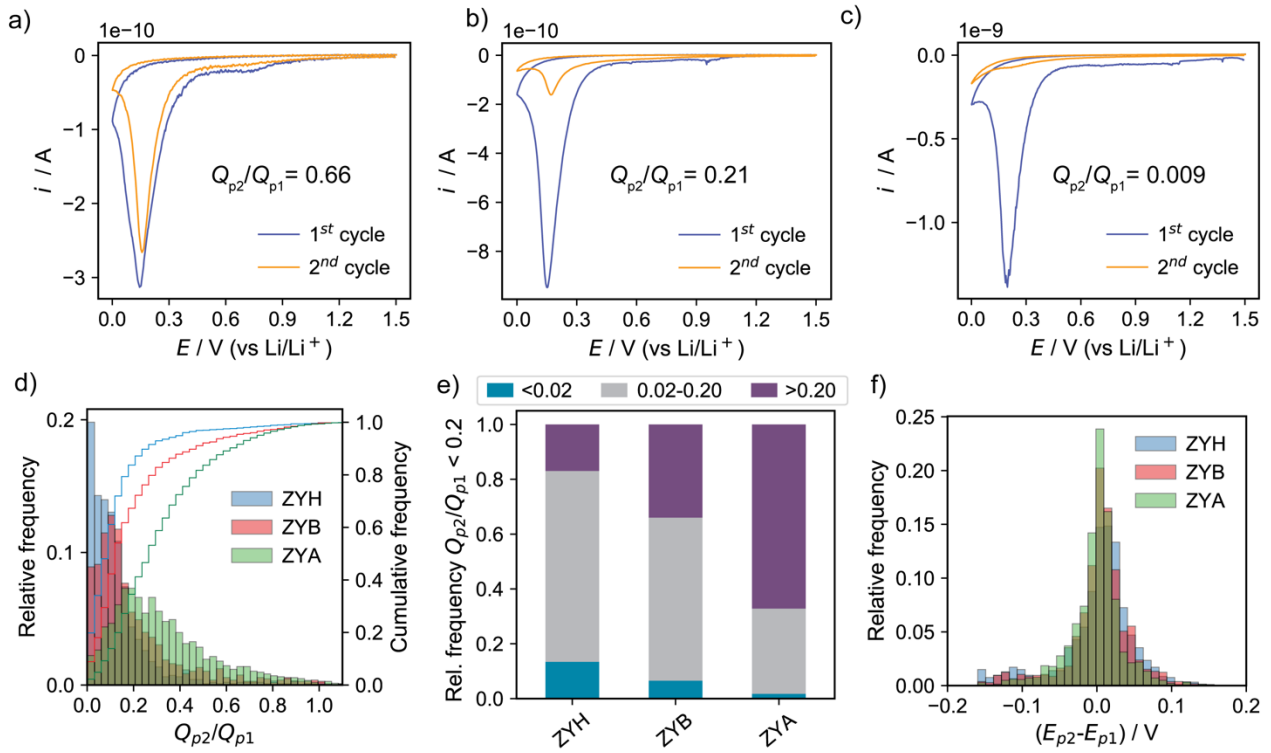


Figure 4. CVs for two cycles (recorded at 3 different locations of ZYB HOPG in 1 M LiPF_6 in EC/EMC at a scan rate of 1 V s^{-1} (1st cycle: blue line, 2nd cycle: orange line). CVs represent locations where different values of Q_{p2}/Q_{p1} (i.e., SEI passivation efficiency) were obtained: (a) 0.66, (b) 0.21, and (c) 0.009. (d) Population analysis illustrating the relative (histogram, left axis) and cumulative (lines, right axis) frequency of SECCM measurements of Q_{p2}/Q_{p1} for HOPG electrodes of different grades: ZYA (green), ZYB (red) and ZYH (blue). The width of the histogram bars is ca. 0.037. (e) Relative frequency of SECCM measurements with Q_{p2}/Q_{p1} values classified as very strongly passivating SEI (< 0.02 , blue), mildly passivating SEI ($0.02-0.20$, grey) and weakly passivating SEI (> 0.20 , purple). (f) Population analysis illustrating the relative frequency of SECCM measurements of $E_{p2}-E_{p1}$ for HOPG electrodes of different grades: ZYA (green), ZYB (red) and ZYH (blue). The width of the histogram bars is ca. 11 mV. Population analyses obtained from 1446, 1061 and 963 independent measurements of ZYA, ZYB and ZYH HOPG, respectively.

The observed differences in passivation efficiency for the different HOPG grades, with lower efficiency at surfaces dominated by smooth terraces, may indicate SEI layers with different characteristics. For instance, the SEI formed on graphite terraces has been found to be less sticky than that formed on step edges,^[19] or can partially dissolve during the reverse voltammetric sweep at potentials as low as $+0.30 \text{ V}$ (vs Li/Li^+)^[63] and to a greater extent on the terraces.^[12] In addition, a thicker SEI is expected to provide more efficient passivation by blocking electron tunnelling and hindering mass transport of electrolyte to the surface. It is reasonable to assume that the thickness of the SEI will scale with the amount of insoluble species formed on the electrode surface, which can thus be correlated to the transferred charge upon electrolyte reduction (Q_{p1}) according to the Faraday's laws of electrolysis. Figure 5 shows a good correlation between Q_{p1} and Q_{p2}/Q_{p1} for the 3 HOPG grades following a quasi-exponential decrease in Q_{p2}/Q_{p1} with increasing Q_{p1} . This

relationship is particularly clear at the boundaries, where the Q_{p2}/Q_{p1} values closer to 1 (low passivation) emanate from low Q_{p1} values, which should generate a relatively small amount of insoluble products on the electrode surface. Similarly, most of the measurements with the largest Q_{p1} for each HOPG electrode, which would generate the largest amount of insoluble products, and thus a thicker SEI layer, correspond to low Q_{p2}/Q_{p1} values (strong passivation efficiency). These results are consistent with the previous observation of a thicker SEI formed on step edges compared to terraces,^[19,56] and provide evidence that the increased SEI thickness and passivating properties is a consequence of the higher electrolyte reduction activity during the first charge/discharge cycle. A similar trend is observed by plotting Q_{p1} vs. Q_{p2} (Figure S7), where the largest Q_{p1} generally tend to result in small Q_{p2} , particularly clear for ZYB and ZYH HOPG surfaces.

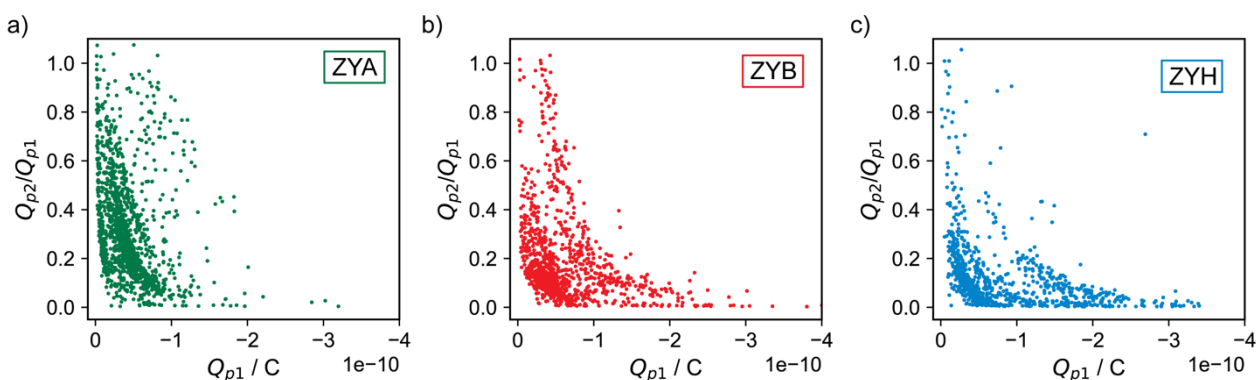


Figure 5. Plots of Q_{p2}/Q_{p1} vs Q_{p1} for a) ZYA, (b) ZYB and (c) ZYH HOPG electrodes. Scan rate: 1 V s⁻¹.

As the SEI causes a significant change to the original electrode surface state, it is worth assessing whether the early stages of the SEI formation can alter the nature of the electrolyte reduction reactions. Electron tunnelling through the SEI layer has been proposed for electrochemical reactions after SEI formation according to a shift in kinetics,^[62] although the thick SEI layers (tens of nm) widely reported^[19,56,63] even in the first charge/discharge formation cycle are not consistent with this observation. Differently, it has been proposed that SEI formation only causes mass transport limitations by either formation of a porous layer or by blocking part of the active electrode area,^[15] but the kinetics of electrochemical reactions remain unaltered. To explore the effect of the formed SEI on electrolyte reduction, two parameters were considered: a) the change in peak potential between the second and first voltammetric cycles ($E_{p2}-E_{p1}$), and b) the change in Tafel slope for the C_{II} reduction process. It is reasonable to expect a change in these values if the reaction is hindered or notably different. The SEI formation did not noticeably affect the peak potentials of the electrolyte reduction since a normal distribution of ($E_{p2}-E_{p1}$) values centred on 0 mV was obtained (Figure 4f) and there was not a clear relationship between the passivation efficiency (Q_{p2}/Q_{p1}) and the corresponding $E_{p2}-E_{p1}$, as shown in Figure S8.

In contrast, interesting information was revealed by analysing the Tafel slope of the C_{II} process. Figure 6 shows this analysis for the same voltammetric curves (first and second cycle) presented in Figure 4a-c, where different SEI passivation efficiencies were observed. Only a small change in the Tafel slope was calculated when the SEI was not strongly passivating. For instance, the Tafel slope changed from 241 to 205 and 178 to 197 mV dec⁻¹ for the cases with Q_{p2}/Q_{p1} of 0.66 and 0.21, respectively (Figure 6a-b). However, when the SEI passivation was strong ($Q_{p2}/Q_{p1} = 0.009$) a significant increase in the Tafel slope was observed (191 to 497 mV dec⁻¹). This behaviour was obtained consistently, as also shown in Figure S9 for another SECCM experiment. It is thus reasonable to conclude that when the SEI passivation is weak or intermediate, electrolyte reduction after SEI formation is similar as for a pristine electrode and the reaction likely takes place directly on the graphite electrode surface without significant changes in kinetics. Thus, the SEI formed under these conditions either has an open porous structure or is not fully covering the electrode surface. Electrolyte reduction through a porous or open structure would be consistent with the theoretical calculations that even a very thin layer (2-3 nm) of inorganic SEI components would prevent electron tunnelling.^[68] A porous structure is also expected for the organic polymeric fraction of the SEI,^[69] and this component also plays an important role in enabling gas bubbles to escape, as ethylene is a significant product of the EC reduction.^[70] In contrast, when the SEI passivation is strong, there is a clear change in Tafel slope for subsequent electrolyte reduction. This might indicate that the reaction does not take place directly on the graphite surface or a different reaction could dominate under these conditions.

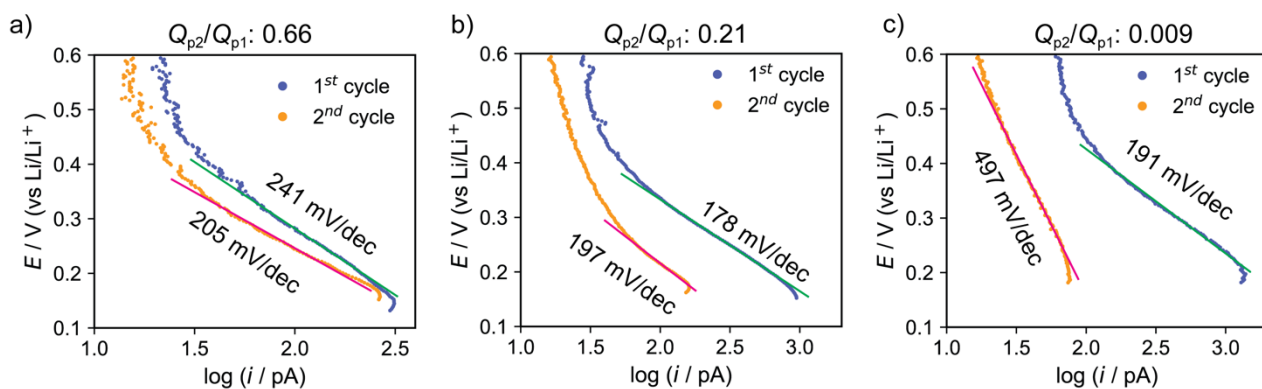


Figure 6. Tafel plots obtained from the electrolyte reduction C_{II} process recorded at 3 different locations of a ZYB HOPG, where different values of Q_{p2}/Q_{p1} (SEI passivation efficiency) were obtained. Full cyclic voltammograms recorded at 1 V s⁻¹ are shown in Figure 3a-c.

Role of cycling rate on the solid-electrolyte interphase formation

Voltammetric SECCM measurements were carried out at different scan rates (0.05, 0.1, 0.2, 0.5, 1 and 2 V s⁻¹) to gain insight on the effect of timescale on the early stages of the SEI formation and the resulting passivation properties through a complete population analysis of the Q_{p2}/Q_{p1} values obtained at different locations of HOPG electrodes. Figures 7a-c show the relative frequency of Q_{p2}/Q_{p1} values classified as the formation of SEI layers with strong ($Q_{p2}/Q_{p1} < 0.2$), medium ($Q_{p2}/Q_{p1} = 0.2-0.60$) and low ($Q_{p2}/Q_{p1} > 0.60$) passivation efficiencies for each HOPG electrode as a function of the scan rate. For all the HOPG grades, faster scan rates tended to produce smaller values of Q_{p2}/Q_{p1} . Additionally, the HOPG structure effect at the wider range of scan rates was similar to that observed at 1 V s⁻¹ with more passivating SEI formed on more defective HOPG electrodes. This is clearly shown in Figure 7d, where the frequency of measurements with Q_{p2}/Q_{p1} values below 0.2 is presented as a function of scan rate and HOPG grade. A good correlation between Q_{p1} absolute values and Q_{p2}/Q_{p1} was also observed at different scan rates (Figure S10), indicating that the extent of electrolyte reduction in the first cycle (indicated by Q_{p1}) also seems to determine the SEI passivation efficiency for each scan rate condition. There is a general trend of increasing Q_{p1} values with increasing scan rates for all the HOPG electrodes, as shown in Figure S11.

It is also important to recognize that the scan rate analysis of Q_{p2}/Q_{p1} is at different scan-rate dependent timescales (longer voltammetric analysis time for slower scan rates). To explore time effects to some extent, SECCM experiments were recorded at 2 V s⁻¹ with a 5 s waiting time (at the starting potential, +1.58 V vs Li/Li⁺) between the first and second cycles on a ZYB HOPG and compared with the experiments recorded uninterruptedly. Figure 8 shows the Q_{p2}/Q_{p1} population analysis for both experiments, showing that measurements with $Q_{p2}/Q_{p1} < 0.15$ (having a strongly passivating SEI) were just 5% of all measurements when the waiting time was applied compared to 93% when continuous cycling carried out. These results reveal that the SEI formed under these conditions evolved with time losing part of its passivation properties, and demonstrate that the timescale is an important parameter to consider when analysing the apparent SEI passivation. In this regard, evaluation of the SEI passivation over increasing number of cycles could provide complementary information about the stability of the SEI components formed in the early stages, as discussed below.

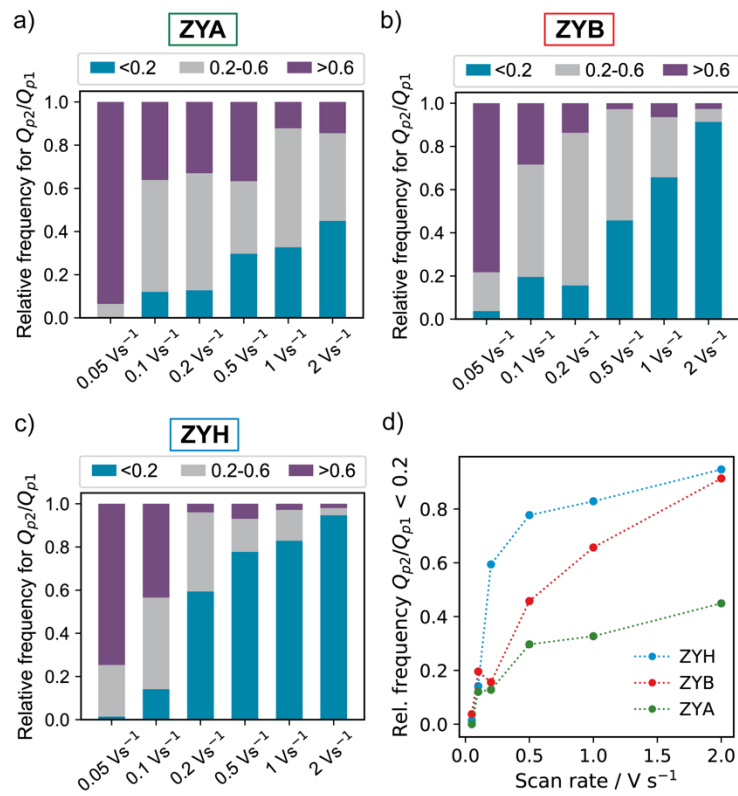


Figure 7. Plots representing the relative frequency of SECCM measurements with Q_{p2}/Q_{p1} values classified as strongly passivating SEI (< 0.2 , blue), mildly passivating SEI ($0.2-0.6$, grey) and weakly passivating SEI (> 0.6 , purple) as a function of scan rate for (a) ZYA, (b) ZYB, and (c) ZYH HOPG electrodes. (d) Relationship between the relative frequency of measurements where a strongly passivation SEI was found ($Q_{p2}/Q_{p1} < 0.2$) and scan rate for ZYA (green), ZYB (red) and ZYH (blue) HOPG electrodes.

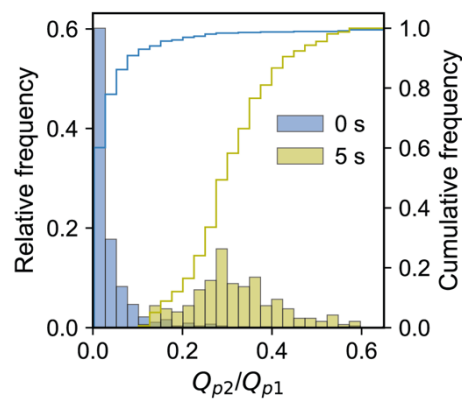


Figure 8. Population analysis representing the relative (histogram, left axis) and cumulative (lines, right axis) frequency of SECCM measurements of Q_{p2}/Q_{p1} , with a 5 s waiting period between the first and second cycle (yellow data), and when cycling took place uninterruptedly (blue data). Data obtained from ZYB HOPG electrodes at a scan rate of 2 V s^{-1} .

Early evolution and stability of the solid-electrolyte interphase

Voltammetric SECCM was carried out similarly to previous experiments but with 5 charge/discharge cycles to reveal the early evolution of the SEI formed on HOPG electrodes under cycling conditions. The peak charge for the electrolyte reduction (C_{II} peak) was integrated for the fifth and second cycles and the ratio (Q_{p5}/Q_{p2}) was considered to evaluate the evolution of the SEI. Figure 9 shows the relative frequency of Q_{p5}/Q_{p2} values classified to represent an SEI layer with less ($Q_{p5}/Q_{p2} < 0.8$), similar ($Q_{p5}/Q_{p2} = 0.8-1.2$) or higher ($Q_{p5}/Q_{p2} > 1.2$) passivation efficiency in the fifth cycle than that found in the second cycle, as a function of the scan rate. Some general conclusions can be reached from these results. For ZYH HOPG, most of the Q_{p5}/Q_{p2} values were below 0.8 for all scan rates, indicating that the SEI layer formed on these electrodes was more passivating with increasing number of cycles. It is not only that a more passivating SEI is initially formed on ZYH HOPG, as discussed in previous sections, but the SEI can block the electrolyte reduction more efficiently upon subsequent cycling. The effect of graphite structure on the SEI evolution can also be quickly identified by comparing the results for different HOPG grades, as shown in Figure 9. In general, the SEI became more passivating with increasing cycles ($Q_{p5}/Q_{p2} < 0.8$) for HOPG electrodes with a more defective surface (ZYB and, especially, ZYH). Structural defects such as step edges seem to promote the formation of a more stable SEI than on smoother surfaces (i.e., terraces), thus allowing a continuous SEI growth upon cycling leading to an apparent more passivating surface.

The specific effect of the scan rate on the SEI evolution is most evident on ZYB and ZYA HOPG. A good fraction of the measurements at fast-intermediate scan rates showed Q_{p5}/Q_{p2} values above 1.2, i.e., a less passivating SEI upon cycling, particularly discernible for ZYA HOPG. This behaviour can be attributed to the initial formation of an unstable SEI, which undergoes some chemical/physical changes allowing further electrolyte reduction in the subsequent cycles (Figure S12a). This behaviour is more important at intermediate scan rates ($0.2 - 1 \text{ V s}^{-1}$), where an unstable SEI would have more time to detach or dissolve from the surface than at faster scan rates such as 2 V s^{-1} .

A different general behaviour was observed at slow scan rates ($< 0.2 \text{ V s}^{-1}$), where most of the measurements presented Q_{p5}/Q_{p2} values below 0.8 for all the HOPG surfaces, indicating a more passivating SEI in the fifth cycle than that detected in the second cycle. In those cases, the SEI formed in the first cycle was not strongly passivating, illustrated by relatively high Q_{p2}/Q_{p1} values as discussed previously, but slow scan rates seem to promote the continuous grow and stabilization of the SEI upon cycling (Figure S12b). There is also a substantial proportion of cases where Q_{p5}/Q_{p2} was below 0.8 at fast scan rates, particularly at 2 V s^{-1} as shown in Figure 9. These cases correspond to surface locations where the SEI formed initially was not totally passivating (Q_{p2}/Q_{p1} was relatively

higher compared to other locations), so the SEI layer still had room to grow and protect the graphite surface more efficiently after the second cycle (Figure S12c).

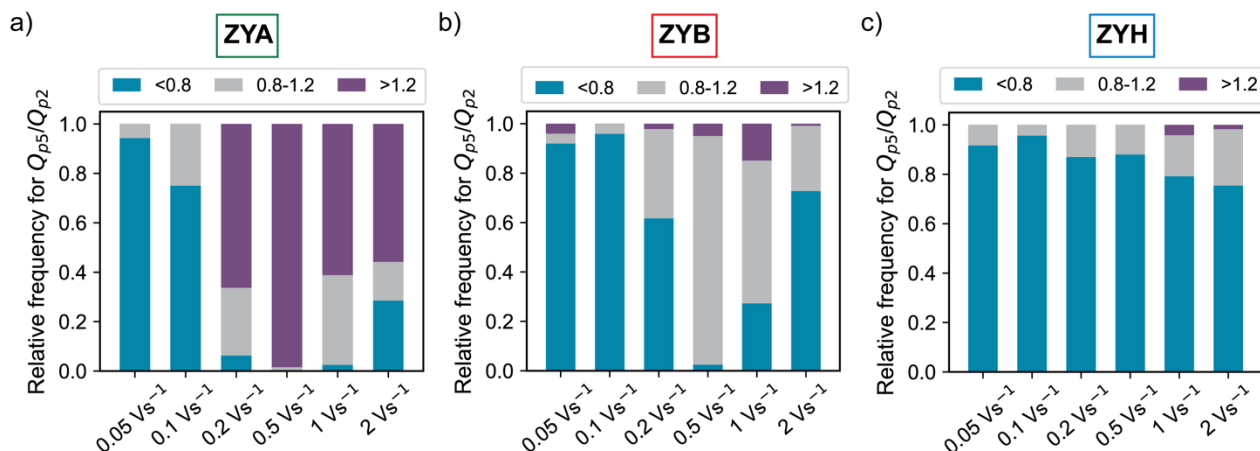


Figure 9. Plots representing the relative frequency of SECCM measurements of Q_{p5}/Q_{p2} values classified as more passivating SEI (< 0.8, blue), similarly passivating SEI (0.8-1.2, grey) and less passivating SEI (> 1.2, purple) in the 5th voltammetric cycle compared to that found in the 2nd cycle, as a function of scan rate for (a) ZYA, (b) ZYB, and (c) ZYH HOPG electrodes.

Thus, the SEI layer initially formed on HOPG electrodes presented strong passivating properties, but relatively low stability, seen at slow and intermediate scan rates in repeat scan measurements, where the insoluble materials have sufficient time to partially detach or dissolve, enabling further electrolyte reduction. This observed time-dependent evolution is consistent with previous studies where the amount of insoluble surface components decreased after the initial SEI formation^[19] and with the fact that SEI compounds can decompose^[71] in presence of $LiPF_6$ leading to some products being either gases or soluble species.^[8,72] However, slower formation rates seem to promote the growth of an increasingly passivating SEI upon cycling, consistent with the wide knowledge of SEI formation strategies where slow rates form a more uniform SEI.^[11,63] Slower formation rates would allow non-stable components to be efficiently removed from the surface and thus sequentially build an SEI formed by the more stable components. In addition, the graphite structure also plays a significant role on the SEI stability, with defective surfaces developing a more stable SEI than smoother graphite, and whose passivation efficiency continuously grows upon cycling even at intermediate-fast scan rates. An SEI mainly consisting of LiF has been reported at low-defective smooth HOPG surfaces,^[23] suggesting that the initially formed organic species could be the non-stable components revealed by our experiments.

CONCLUSIONS

High volume, spatially-resolved SECCM in a glovebox was employed to provide large datasets, in order to characterize SEI formation and properties for model graphite electrodes with different grades of structural defects. More defective graphite structures, where a high electroactivity for electrolyte reduction was observed on the original electrode surface, can promote a more passivating and stable SEI, thus preventing further electrolyte reactivity and consumption upon cycling. The rapid formation of a strongly passivating SEI was detected at very fast scan rates. However, the SEI formed under these conditions appears to be comprised of non-stable components and an evident future goal would be the development of strategies to preserve these early SEI components, since they prevent further electrolyte consumption efficiently. Controlling the material structure would be the clearest scenario, as our results show that graphite with a higher coverage of defects (step edges) promoted the formation of a more stable and strongly passivating SEI compared to smoother surfaces. Identification of the early SEI components, generated under these conditions, is worthy of further investigation towards developing improved (faster) SEI formation methods, one of the main bottlenecks during LiB manufacturing.

We anticipate that correlative electrochemical microscopy, combining the demonstrated features of high-throughput SECCM, coupled with other microscopy and spectroscopy techniques, will be a significant approach to truly understand battery processes taking place on heterogeneous materials of practical importance. This study is a first step towards this goal, demonstrating the viability of SECCM measurements in a glovebox environment, with the next target being high-resolution electrochemical imaging of battery materials.

EXPERIMENTAL SECTION

Chemicals and electrode materials

Battery-grade lithium hexafluorophosphate solution in ethylene carbonate (EC) and ethyl methyl carbonate (1.0 M LiPF₆ in EC/EMC=50/50 (v/v); Sigma-Aldrich) was used as received. This solution contained <15 ppm of H₂O and <50 ppm of HF according to the manufacturer. Ferrocene (Fc) (98%) was also obtained from Sigma-Aldrich.

HOPG electrodes of different crystallographic quality with a mosaic spread of $0.4^{\circ}\pm 0.1^{\circ}$ (ZYA), $0.8^{\circ}\pm 0.2^{\circ}$ (ZYP) and $3.5^{\circ}\pm 1.5^{\circ}$ (ZYH) according to the manufacturer, were obtained from Scanwel. The HOPG electrodes were fixed to stainless-steel AFM specimen disks (Agar Scientific) and electrically connected through conductive silver paint (RS Supplies). Samples were transferred into the glovebox and stored in a closed container under inert atmosphere. HOPG electrodes were freshly cleaved with adhesive tape immediately prior to the SECCM experiments to peel back the top

layer and uncover a clean surface, as surface aging has been shown to affect HOPG electrochemistry.^[73]

Ag wires (0.25 mm diameter, 99.99%, Goodfellow) were used as quasi-reference counter electrodes (QRCEs). Ag QRCEs have been previously used successfully for long-term (> 30 h) electrochemical microscopy experiments of Li-ion battery materials.^[36] The Ag QRCE potential was converted to the Li/Li⁺ scale after calibration against the IUPAC recommended Fc/Fc⁺ process,^[74] which is known to occur at a potential of ca. +3.25 V vs Li/Li⁺ in 1 M LiPF₆ in EC/EMC (1:1).^[75] Fc electro-oxidation had a reversible half-wave potential, $E_{1/2}$, of +0.17 V vs Ag QRCE as shown in Figure S2.

Scanning electrochemical cell microscopy (SECCM)

Electrochemical experiments were made using SECCM as schematized in Figure 1a-b. A home-built SECCM instrument, as previously reported,^[40,45,52] which was installed in an Ar-filled glovebox (MBraun MB200B/MB20G); H₂O and O₂ levels < 0.1 ppm. Single-barrel pipette probes (tip diameter of ~500 nm, Figure S1a) were prepared by pulling borosilicate filamented capillaries with a 1.2 mm outer diameter and a 0.69 mm inner diameter (GC120F-10, Harvard Apparatus) using a CO₂-laser puller (P-2000, Sutter Instruments). Larger pipette probes (ca. 30 μ m diameter, Figure S1b) prepared with a PC-10 puller (Narishige Group) were also used in a specific experiment. Puller programs to fabricate both pipette probes are described in SI, Section S2. 3D-printed pipette holders (Figure 1c) were designed and fabricated in order to facilitate the handling, filling and mounting of the pipettes on the SECCM positioner inside the glovebox. Pipettes were backfilled with electrolyte solution using a MicroFil syringe (MF34G-5, World Precision Instruments) and the Ag QRCE was then inserted into the pipette, leaving at least 3 cm of separation of the end of the wire to the pipette tip.^[76] The pipette probe was then mounted on a 3-axis xyz piezoelectric positioner (P-611.3S, NanoCube, Physik Instruments) and was positioned near the HOPG surface, as shown in Figure 1d, by coarse adjustment with assistance of an optical camera (PL-B782U, 2X lens, Pixelink). Experiments were carried out in visually smooth HOPG areas, avoiding large steps and defects. The SECCM setup (sample, positioner and camera) was placed on a vibration isolation platform (BM-10, Minus K Technology) to minimize mechanical vibrations and was covered with a copper woven mesh (60 mesh per inch, 0.16 mm wire diameter, Cadisch Precision Meshes) acting as a Faraday cage to reduce electrical noise. The optical camera USB was connected to ground during the experiments.

SECCM experiments were carried out using a cyclic voltammetry (CV) hopping-mode protocol (Figure 1a-b) as previously reported.^[45,77] The pipette probe was approached to the HOPG surface by the piezoelectric positioner at a speed of 3 μ m s⁻¹. A surface current (i_{surf}) threshold of 2.0 pA (applied bias of +1.58 V to the HOPG vs Li/Li⁺ (-1.50 V vs Ag QRCE)) was selected to detect

when contact between the probe liquid meniscus and the HOPG was made, to stop further movement of the pipette. In this way, a confined liquid cell was created between the pipette probe and the HOPG surface, but the probe itself never contacted the surface. For the voltammetric analysis, a potential sweep was applied to the HOPG electrode by controlling the QRCE potential held at a common ground and the surface current (i_{surf}) flowing through both electrodes was recorded by a custom-built electrometer. A data acquisition rate of 2570 μs was employed, where the current was measured every 10 μs and averaged 256 times with one extra iteration for transferring data to the computer.

After the voltammetric data were recorded in one position, the probe was retracted from the surface at a speed of 5 $\mu\text{m s}^{-1}$ (typically 6 μm in the z-axis) and translated at the same speed to the next location to repeat the approach-measure-retract steps until a predefined array of grid points had been covered across the surface. To prevent spatial overlap of the measurements, the hopping spots were separated by 5 or 8 μm in the xy plane. An optical image of the droplet footprints left on the HOPG surface after a typical SECCM experiment with a ca. 500 nm diameter probe containing 1 M LiPF_6 in EC/EMC is shown in Figure 1e. Well-defined and highly consistent footprints are obtained, which proves that the meniscus contact with the HOPG surface is very stable under the working conditions in the glovebox.

Data acquisition and instrumental control in SECCM was carried out using a FPGA card (NI PCIe-7852R) controlled by a LabVIEW 2020 (National Instruments) interface running the Warwick electrochemical scanning probe microscopy (WEC-SPM, www.warwick.ac.uk/electrochemistry) software. Data processing and analysis was carried out with a code written in-house in Python language with the aid of SciPy libraries.^[78] Analysed data were obtained from SECCM scans repeated on different days, using freshly prepared pipette probes and freshly cleaved HOPG surfaces.

Surface characterization

Optical microscopy (OM) images of the SECCM droplet footprints were recorded with an upright Olympus BH2 optical microscope (reflection mode) equipped with an optical camera (PL-B782U, 4X lens, Pixelink). Atomic force microscopy (AFM) was carried out using an Innova atomic force microscope (Bruker) in tapping mode with Antimony (n) doped Si probes (RFESP-75, Bruker). Scans were recorded with 256 points per line at 0.1 Hz over (5x5) μm^2 of the HOPG electrode area. AFM images were analysed with the Gwyddion software (v2.55, Czech Metrology Institute). Nanopipette probes were imaged by scanning electron microscopy (SEM) on a GeminiSEM 500 instrument (Zeiss).

ACKNOWLEDGMENTS

This work was supported by the UK Faraday Institution (EP/S003053/1) through the Characterisation project (FIRG013). PRU thanks the Royal Society for a Wolfson Research Merit Award. We would like to thank Joshua Tully for printing the 3D-printed nanopipette holders and Xiangdong Xu for recording the SEM images of nanopipettes.

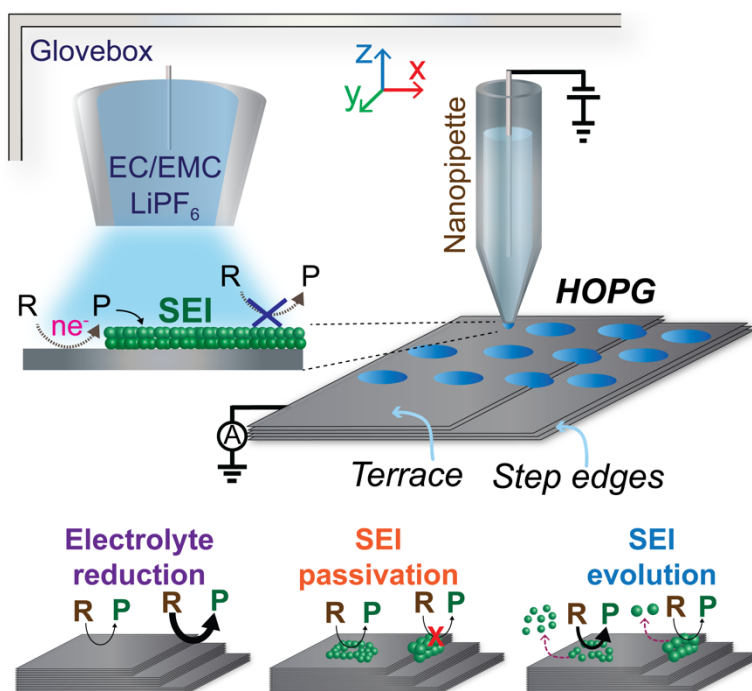
REFERENCES

- [1] E. Peled, *J. Electrochem. Soc.* **1979**, *126*, 2047.
- [2] K. Xu, *Chem. Rev.* **2014**, *114*, 11503–11618.
- [3] S. J. An, J. Li, C. Daniel, D. Mohanty, S. Nagpure, D. L. Wood, *Carbon* **2016**, *105*, 52–76.
- [4] J. Asenbauer, T. Eisenmann, M. Kuenzel, A. Kazzazi, Z. Chen, D. Bresser, *Sustain. Energy Fuels* **2020**, *4*, 5387–5416.
- [5] V. A. Agubra, J. W. Fergus, *J. Power Sources* **2014**, *268*, 153–162.
- [6] D. L. Wood, J. Li, C. Daniel, *J. Power Sources* **2015**, *275*, 234–242.
- [7] M. B. Pinson, M. Z. Bazant, *J. Electrochem. Soc.* **2013**, *160*, A243–A250.
- [8] S. K. Heiskanen, J. Kim, B. L. Lucht, *Joule* **2019**, *3*, 2322–2333.
- [9] I. Weber, B. Wang, C. Bodirsky, M. Chakraborty, M. Wachtler, T. Diemant, J. Schnaidt, R. J. Behm, *ChemElectroChem* **2020**, *7*, 4794–4809.
- [10] Y. Chu, Y. Shen, F. Guo, X. Zhao, Q. Dong, Q. Zhang, W. Li, H. Chen, Z. Luo, L. Chen, *Electrochem. Energy Rev.* **2019**, DOI 10.1007/s41918-019-00058-y.
- [11] T. Zhu, Q. Hu, G. Yan, J. Wang, Z. Wang, H. Guo, X. Li, W. Peng, *Energy Technol.* **2019**, *7*, 1900273.
- [12] Z. Zhang, K. Smith, R. Jervis, P. R. Shearing, T. S. Miller, D. J. L. Brett, *ACS Appl. Mater. Interfaces* **2020**, *12*, 35132–35141.
- [13] D. Aurbach, H. Teller, E. Levi, *J. Electrochem. Soc.* **2002**, *149*, A1255.
- [14] D. Aurbach, H. Teller, M. Koltypin, E. Levi, *J. Power Sources* **2003**, *119–121*, 2–7.
- [15] M. Tang, K. Miyazaki, T. Abe, J. Newman, *J. Electrochem. Soc.* **2012**, *159*, A634–A641.
- [16] E. Peled, D. Golodnitsky, A. Ulus, V. Yufit, *Electrochimica Acta* **2004**, *50*, 391–395.
- [17] K. Persson, V. A. Sethuraman, L. J. Hardwick, Y. Hinuma, Y. S. Meng, A. van der Ven, V. Srinivasan, R. Kostecki, G. Ceder, *J. Phys. Chem. Lett.* **2010**, *1*, 1176–1180.
- [18] A. v. Cresce, S. M. Russell, D. R. Baker, K. J. Gaskell, K. Xu, *Nano Lett.* **2014**, *14*, 1405–1412.
- [19] S. Yu. Luchkin, S. A. Lipovskikh, N. S. Katorova, A. A. Savina, A. M. Abakumov, K. J. Stevenson, *Sci. Rep.* **2020**, *10*, 8550.
- [20] Y. Domi, M. Ochida, S. Tsubouchi, H. Nakagawa, T. Yamanaka, T. Doi, T. Abe, Z. Ogumi, *J. Phys. Chem. C* **2011**, *115*, 25484–25489.
- [21] Y. Yamada, K. Miyazaki, T. Abe, *Langmuir* **2010**, *26*, 14990–14994.
- [22] Y. NuLi, J. Yang, Z. Jiang, *J. Phys. Chem. Solids* **2006**, *67*, 882–886.
- [23] I. Weber, J. Schnaidt, B. Wang, T. Diemant, R. J. Behm, *ChemElectroChem* **2019**, *6*, 4985–4997.
- [24] Y. Shi, H.-J. Yan, R. Wen, L.-J. Wan, *ACS Appl. Mater. Interfaces* **2017**, *9*, 22063–22067.
- [25] Y. Domi, T. Doi, S. Tsubouchi, T. Yamanaka, T. Abe, Z. Ogumi, *Phys. Chem. Chem. Phys.* **2016**, *18*, 22426–22433.
- [26] C. Shen, S. Wang, Y. Jin, W.-Q. Han, *ACS Appl. Mater. Interfaces* **2015**, *7*, 25441–25447.
- [27] L. Wang, X. Deng, P.-X. Dai, Y.-G. Guo, D. Wang, L.-J. Wan, *Phys. Chem. Chem. Phys.* **2012**, *14*, 7330.
- [28] L. Seidl, S. Martens, J. Ma, U. Stimming, O. Schneider, *Nanoscale* **2016**, *8*, 14004–14014.

- [29] L. Wang, D. Deng, L. C. Lev, S. Ng, *J. Power Sources* **2014**, *265*, 140–148.
- [30] H. Bülter, F. Peters, G. Wittstock, *Energy Technol.* **2016**, *4*, 1486–1494.
- [31] G. Zampardi, F. La Mantia, W. Schuhmann, *RSC Adv.* **2015**, *5*, 31166–31171.
- [32] G. Zampardi, S. Klink, V. Kuznetsov, T. Erichsen, A. Maljusch, F. La Mantia, W. Schuhmann, E. Ventosa, *ChemElectroChem* **2015**, *2*, 1607–1611.
- [33] J. Hui, M. Burgess, J. Zhang, J. Rodríguez-López, *ACS Nano* **2016**, *10*, 4248–4257.
- [34] X. Zeng, D. Liu, S. Wang, S. Liu, X. Cai, L. Zhang, R. Zhao, B. Li, F. Kang, *ACS Appl. Mater. Interfaces* **2020**, *12*, 37047–37053.
- [35] H. Bülter, P. Schwager, D. Fenske, G. Wittstock, *Electrochimica Acta* **2016**, *199*, 366–379.
- [36] H. Bülter, F. Peters, J. Schwenzel, G. Wittstock, *Angew. Chem. Int. Ed.* **2014**, *53*, 10531–10535.
- [37] E. dos Santos Sardinha, M. Sternad, H. M. R. Wilkening, G. Wittstock, *ACS Appl. Energy Mater.* **2019**, *2*, 1388–1392.
- [38] N. Ebejer, M. Schnippering, A. W. Colburn, M. A. Edwards, P. R. Unwin, *Anal. Chem.* **2010**, *82*, 9141–9145.
- [39] M. E. Snowden, A. G. Güell, S. C. S. Lai, K. McKelvey, N. Ebejer, M. A. O’Connell, A. W. Colburn, P. R. Unwin, *Anal. Chem.* **2012**, *84*, 2483–2491.
- [40] C. L. Bentley, M. Kang, P. R. Unwin, *Curr. Opin. Electrochem.* **2017**, *6*, 23–30.
- [41] O. J. Wahab, M. Kang, P. R. Unwin, *Curr. Opin. Electrochem.* **2020**, *22*, 120–128.
- [42] C. L. Bentley, C. Andronesco, M. Smialkowski, M. Kang, T. Tarnev, B. Marler, P. R. Unwin, U.-P. Apfel, W. Schuhmann, *Angew. Chem. Int. Ed.* **2018**, *57*, 4093–4097.
- [43] J. T. Mefford, A. R. Akbashev, M. Kang, C. L. Bentley, W. E. Gent, H. D. Deng, D. H. Alsem, Y.-S. Yu, N. J. Salmon, D. A. Shapiro, P. R. Unwin, W. C. Chueh, *Nature* **2021**, *593*, 67–73.
- [44] L. C. Yule, V. Shkirskiy, J. Aarons, G. West, C. L. Bentley, B. A. Shollock, P. R. Unwin, *J. Phys. Chem. C* **2019**, *123*, 24146–24155.
- [45] D. Martín-Yerga, A. Costa-García, P. R. Unwin, *ACS Sens.* **2019**, *4*, 2173–2180.
- [46] Y. Takahashi, A. Kumatani, H. Munakata, H. Inomata, K. Ito, K. Ino, H. Shiku, P. R. Unwin, Y. E. Korchev, K. Kanamura, T. Matsue, *Nat. Commun.* **2014**, *5*, 5450.
- [47] A. Kumatani, Y. Takahashi, C. Miura, H. Ida, H. Inomata, H. Shiku, H. Munakata, K. Kanamura, T. Matsue, *Surf. Interface Anal.* **2019**, *51*, 27–30.
- [48] B. Tao, L. C. Yule, E. Daviddi, C. L. Bentley, P. R. Unwin, *Angew. Chem. Int. Ed.* **2019**, *58*, 4606–4611.
- [49] M. Dayeh, M. R. Z. Ghavidel, J. Mauzeroll, S. B. Schougaard, *ChemElectroChem* **2019**, *6*, 195–201.
- [50] M. E. Snowden, M. Dayeh, N. A. Payne, S. Gervais, J. Mauzeroll, S. B. Schougaard, *J. Power Sources* **2016**, *325*, 682–689.
- [51] S. P. E, M. Kang, P. Wilson, L. Meng, D. Perry, A. Basile, P. R. Unwin, *Chem. Commun.* **2018**, *54*, 3053–3056.
- [52] C. L. Bentley, M. Kang, P. R. Unwin, *Anal. Chem.* **2020**, *92*, 11673–11680.
- [53] Y. Takahashi, T. Yamashita, D. Takamatsu, A. Kumatani, T. Fukuma, *Chem. Commun.* **2020**, *56*, 9324–9327.
- [54] Hsiangpin. Chang, A. J. Bard, *Langmuir* **1991**, *7*, 1143–1153.
- [55] L. Wang, A. Menakath, F. Han, Y. Wang, P. Y. Zavalij, K. J. Gaskell, O. Borodin, D. Iuga, S. P. Brown, C. Wang, K. Xu, B. W. Eichhorn, *Nat. Chem.* **2019**, *11*, 789–796.
- [56] M. Nie, D. Chalasani, D. P. Abraham, Y. Chen, A. Bose, B. L. Lucht, *J. Phys. Chem. C* **2013**, *117*, 1257–1267.
- [57] Y. Wang, S. Nakamura, M. Ue, P. B. Balbuena, *J. Am. Chem. Soc.* **2001**, *123*, 11708–11718.
- [58] D. M. Seo, D. Chalasani, B. S. Parimalam, R. Kadam, M. Nie, B. L. Lucht, *ECS Electrochem. Lett.* **2014**, *3*.
- [59] K. Xu, *Chem. Rev.* **2004**, *104*, 4303–4418.

- [60] D. Strmcnik, I. E. Castelli, J. G. Connell, D. Haering, M. Zorko, P. Martins, P. P. Lopes, B. Genorio, T. Østergaard, H. A. Gasteiger, F. Maglia, B. K. Antonopoulos, V. R. Stamenkovic, J. Rossmeisl, N. M. Markovic, *Nat. Catal.* **2018**, *1*, 255–262.
- [61] G. V. Zhuang, K. Xu, H. Yang, T. R. Jow, P. N. Ross, *J. Phys. Chem. B* **2005**, *109*, 17567–17573.
- [62] B. K. Antonopoulos, F. Maglia, F. Schmidt-Stein, J. P. Schmidt, H. E. Hoster, *Batter. Supercaps* **2018**, *1*, 110–121.
- [63] T. Liu, L. Lin, X. Bi, L. Tian, K. Yang, J. Liu, M. Li, Z. Chen, J. Lu, K. Amine, K. Xu, F. Pan, *Nat. Nanotechnol.* **2019**, *14*, 50–56.
- [64] E. Peled, S. Menkin, *J. Electrochem. Soc.* **2017**, *164*, A1703–A1719.
- [65] K. Edström, M. Herstedt, D. P. Abraham, *J. Power Sources* **2006**, *153*, 380–384.
- [66] E. Peled, *J. Power Sources* **2001**, *6*.
- [67] J. Zou, C. Sole, N. E. Drewett, M. Velický, L. J. Hardwick, *J. Phys. Chem. Lett.* **2016**, *7*, 4291–4296.
- [68] A. Wang, S. Kadam, H. Li, S. Shi, Y. Qi, *Npj Comput. Mater.* **2018**, *4*, 15.
- [69] P. Guan, L. Liu, X. Lin, *J. Electrochem. Soc.* **2015**, *162*, A1798–A1808.
- [70] U. Mattinen, M. Klett, G. Lindbergh, R. Wreland Lindström, *J. Power Sources* **2020**, *477*, 228968.
- [71] M. Tang, J. Newman, *J. Electrochem. Soc.* **2012**, *159*, A1922–A1927.
- [72] B. S. Parimalam, A. D. MacIntosh, R. Kadam, B. L. Lucht, *J. Phys. Chem. C* **2017**, *121*, 22733–22738.
- [73] A. N. Patel, M. G. Collignon, M. A. O’Connell, W. O. Y. Hung, K. McKelvey, J. V. Macpherson, P. R. Unwin, *J. Am. Chem. Soc.* **2012**, *134*, 20117–20130.
- [74] G. Gritzner, J. Kůta, *Electrochimica Acta* **1984**, *29*, 869–873.
- [75] C. O. Laoire, E. Plichta, M. Hendrickson, S. Mukerjee, K. M. Abraham, *Electrochimica Acta* **2009**, *54*, 6560–6564.
- [76] C. L. Bentley, D. Perry, P. R. Unwin, *Anal. Chem.* **2018**, *90*, 7700–7707.
- [77] C.-H. Chen, L. Jacobse, K. McKelvey, S. C. S. Lai, M. T. M. Koper, P. R. Unwin, *Anal. Chem.* **2015**, *87*, 5782–5789.
- [78] SciPy 1.0 Contributors, P. Virtanen, R. Gommers, T. E. Oliphant, M. Haberland, T. Reddy, D. Cournapeau, E. Burovski, P. Peterson, W. Weckesser, J. Bright, S. J. van der Walt, M. Brett, J. Wilson, K. J. Millman, N. Mayorov, A. R. J. Nelson, E. Jones, R. Kern, E. Larson, C. J. Carey, Í. Polat, Y. Feng, E. W. Moore, J. VanderPlas, D. Laxalde, J. Perktold, R. Cimrman, I. Henriksen, E. A. Quintero, C. R. Harris, A. M. Archibald, A. H. Ribeiro, F. Pedregosa, P. van Mulbregt, *Nat. Methods* **2020**, *17*, 261–272.

TABLE OF CONTENTS GRAPHIC



Surface heterogeneity and structural defects in the basal plane of graphite affect the early stages of the solid-electrolyte interphase (SEI) formation and its properties in a Li-ion battery electrolyte, as revealed by scanning electrochemical cell microscopy (SECCM) in a glovebox.